



Top-seeded solid-state single crystal growth of $0.75(\text{Na}_{0.5}\text{Bi}_{0.5})\text{TiO}_3$ - 0.25SrTiO_3 single crystals in oxygen and their characterization

Phan Gia Le^{1,2,6} · Jong-Sook Lee¹ · Hwang-Pill Kim³ · Wook Jo³ · Hang Xie⁴ · Yunfei Chang⁴ · Wenwei Ge⁵ · John G. Fisher¹

Received: 11 March 2024 / Revised: 14 May 2024 / Accepted: 6 June 2024
© The Korean Ceramic Society 2024

Abstract

In this present work, $0.75(\text{Na}_{0.5}\text{Bi}_{0.5})\text{TiO}_3$ - 0.25SrTiO_3 single crystals were grown by top-seeded solid-state crystal growth under an oxygen atmosphere. Growth in oxygen resulted in improved single-crystal growth and density compared to single crystals previously grown in air. X-ray diffraction revealed the simultaneous presence of tetragonal and cubic phases in the crystal while Raman scattering suggested the presence of rhombohedral and tetragonal phases. Piezoresponse force microscopy and electrostatic force microscopy show that the single crystal is in an ergodic relaxor state and electrostatic force microscopy shows that ferroelectric domains can be induced by an electric field. Dielectric property measurements show behaviour typical of an $(\text{Na}_{0.5}\text{Bi}_{0.5})\text{TiO}_3$ -type relaxor material. Polarization and strain vs. electric field hysteresis measurements show that the single crystal is an incipient ferroelectric. A maximum strain of 0.48% was obtained at an electric field of 3.5 kV/mm, giving $S_{\text{max}}/E_{\text{max}} = 1365$ pm/V, which is an enhancement of 32% compared to $0.75(\text{Na}_{0.5}\text{Bi}_{0.5})\text{TiO}_3$ - 0.25SrTiO_3 single crystals grown in air.

Keywords $(\text{Na}_{0.5}\text{Bi}_{0.5})\text{TiO}_3$ · Single crystal · Piezoelectric properties · Ferroelectric properties · Actuators

✉ John G. Fisher
johnfisher@jnu.ac.kr

¹ School of Materials Science and Engineering, Chonnam National University, 77 Yongbong-ro, Buk-gu, Gwangju 61186, Republic of Korea

² Department of BioNano Technology, Gachon University, 1342 Seongnamdaero, Sujeong-gu, Seongnam-Si, Gyeonggi-Do 13120, Republic of Korea

³ School of Materials Science and Engineering, Ulsan National Institute of Science and Technology, Unist-gil 50, Eonyang-Eup, Ulju-gun, Ulsan 44919, Republic of Korea

⁴ Functional Materials and Acousto-Optic Instruments Institute, School of Instrumentation Science and Engineering, Harbin Institute of Technology, Harbin 150080, People's Republic of China

⁵ Key Laboratory of Automobile Materials, School of Materials Science and Engineering, Jilin University, Changchun, Jilin 130022, People's Republic of China

⁶ Present Address: Department of Electronic Engineering, Gachon University, Seongnam-si, Gyeonggi-do 13120, Republic of Korea

1 Introduction

Recently, $0.75(\text{Na}_{0.5}\text{Bi}_{0.5})\text{TiO}_3$ - 0.25SrTiO_3 ceramics, with a phase boundary between rhombohedral and tetragonal or pseudocubic phases, have been receiving much attention from scientists in the piezoelectric materials research area, owing to their outstanding inverse piezoelectrical properties, which are caused by a phase transition under an applied electric field [1–8]. $(\text{Na}_{0.5}\text{Bi}_{0.5})\text{TiO}_3$ -based materials are being considered as a substitute for $\text{Pb}(\text{Zr},\text{Ti})\text{O}_3$ commercial products due to the need to reduce the toxicity of piezoelectric materials, prevent environmental pollution, and improve the health of human beings [5, 9–13]. The $(\text{Na}_{0.5}\text{Bi}_{0.5})\text{TiO}_3$ - SrTiO_3 system may play a key role for electronic components based on the piezoelectric actuator application [14, 15]. Hence, the study of the $0.75(\text{Na}_{0.5}\text{Bi}_{0.5})\text{TiO}_3$ - 0.25SrTiO_3 system is of great significance for discovering lead-free piezoelectric materials to replace $\text{Pb}(\text{Zr},\text{Ti})\text{O}_3$.

Based on many publications, $0.75(\text{Na}_{0.5}\text{Bi}_{0.5})\text{TiO}_3$ - 0.25SrTiO_3 and related compositions have been studied and investigated in powder [16, 17], polycrystalline bulk ceramic [1, 2, 5, 7, 8, 17, 18], thin film [19, 20] and single

crystalline [21, 22] states. This research concentrated on improving the electrical properties, namely higher inverse piezoelectric constant, slimmer hysteresis loops to improve actuating precision, and faster response rate for piezoelectric actuator application. On the one hand, the base composition was designed and modified with the involvement of other foreign elements and compounds as dopants or components to modify the electrical properties [14, 23–25], while on the other hand, the base composition was retained, whilst core–shell engineering [16, 17, 24, 26, 27] or texturing [28] has been used. Normally, polycrystalline piezoelectric ceramics consist of grains arranged in various crystallographic orientations, which limits the degree of orientation of the ferroelectric domains under an applied electric field, making the poling of the ceramic less efficient. This is accompanied by reduced piezoelectric properties. To overcome this limitation, single crystals can be used. The crystal's crystallographic orientation can be arranged to maximize domain realignment during poling, improving the electrical properties [29, 30]. Among many techniques for single crystal growth, such as Bridgman [31–34], top-seeded-solution-growth [35, 36], flux-growth [37–39], solid-state crystal growth [22, 23, 40–46], etc., the solid-state crystal growth technique has several advantages such as the ability to produce a single crystal using commonly-available laboratory equipment, avoidance of contamination, reduction of evaporation of volatile elements, and improved control of composition stoichiometry [47, 48]. Thus, in this current work, solid-state single-crystal growth was employed to grow single crystals of $0.75(\text{Na}_{0.5}\text{Bi}_{0.5})\text{TiO}_3\text{-}0.25\text{SrTiO}_3$.

Optimization of single crystal growth conditions is a key factor for control of the electrical properties, which is necessary for practical applications. In previous work on solid-state crystal growth in this system, the effect of growth temperature, time [21, 22] and composition [23, 40] was studied. Single crystals with thicknesses on the millimeter scale were grown with superior inverse piezoelectric properties to the equivalent polycrystalline ceramics ($S_{\text{max}}/E_{\text{max}} = 1042$ pm/V vs. 739 pm/V and $\Delta S/S_{\text{max}} = 38.7$ vs. 57.1%) [22]. However, the single crystals were very porous, which is a major obstacle for further enhancement of the electrical properties. Control of the sintering atmosphere is one way of improving the density of ceramics as well as the electrical properties. Previous investigations have shown that sintering (Pb,La)(Zr,Ti)O₃ ceramics in an oxygen atmosphere can be beneficial in reducing porosity [49, 50]. Spreitzer et al. found that sintering $(1-x)(\text{Na}_{0.5}\text{Bi}_{0.5})\text{TiO}_3\text{-}x\text{SrTiO}_3$ ceramics under an oxygen pressure of 1 MPa was beneficial for improving phase purity and density [51]. Sintering under high oxygen pressure suppressed the evaporation of secondary phases and allowed a higher sintering temperature to be used. This promoted densification and conversion of the secondary phases into the matrix phase. Liu et al. found that sintering $0.66(\text{Na}_{0.5}\text{Bi}_{0.5})$

$\text{TiO}_3\text{-}0.06\text{BaTiO}_3\text{-}0.28(\text{Bi}_x\text{Sr}_{1-3x/2}\square_{x/2})\text{TiO}_3$ in oxygen promoted densification, reduced grain size and improved electrical properties (increased resistivity and energy storage efficiency) due to the reduced formation of oxygen vacancies [52]. Oxygen vacancies are believed to affect the conductivity and high-temperature dielectric behaviour of $(\text{Na}_{0.5}\text{Bi}_{0.5})\text{TiO}_3$ -based ceramics and single crystals [53–58]. Growth of $(\text{Na}_{0.5}\text{Bi}_{0.5})\text{TiO}_3$ -based single crystals by flux and top-seeded solution growth methods in an oxygen atmosphere was found to reduce leakage current and improve electrical properties [59–62]. It is possible that solid-state crystal growth of $0.75(\text{Na}_{0.5}\text{Bi}_{0.5})\text{TiO}_3\text{-}0.25\text{SrTiO}_3$ single crystals in an oxygen atmosphere could reduce porosity and improve electrical properties even further.

In the current work, $0.75(\text{Na}_{0.5}\text{Bi}_{0.5})\text{TiO}_3\text{-}0.25\text{SrTiO}_3$ single crystals were produced by top-seeded solid-state crystal growth in an oxygen atmosphere. The structure of the attained single crystals was characterized by X-ray diffraction and Raman scattering. Ferroelectric domain structure was studied by piezoresponse force microscopy (PFM) and electrostatic force microscopy (EFM). Electrical properties were studied using impedance spectroscopy and measurement of the polarization and strain vs. electric field hysteresis loops.

2 Materials and methods

The $0.75(\text{Na}_{0.5}\text{Bi}_{0.5})\text{TiO}_3\text{-}0.25\text{SrTiO}_3$ (NBT-25ST) powder is prepared from Na_2CO_3 (ACROS organics, 99.5%), Bi_2O_3 (Alfa Aesar, 99.9%), SrCO_3 (Aldrich, $\geq 99.9\%$) and TiO_2 (Alfa Aesar, 99.8%) precursor materials by the mixed oxide method [21]. Single crystal growth experiments were performed by top-seeded solid-state crystal growth. Approx. 0.3 g of NBT-25ST powder (without a seed crystal) was hand-pressed into a pellet in a 6 mm diameter stainless-steel die, followed by cold isostatic pressing at 50 MPa. The pellet was pre-sintered in oxygen for 1 h at 900 °C, with 5 °C.min⁻¹ heating and cooling rates. One face of the pellet was polished to a 1 μm finish using diamond suspension. Then 0.2 g of NBT-25ST packing powder was lightly pressed by hand in a stainless-steel die of 10 mm diameter. The pellet was placed in the die polished face up and a [110]-oriented SrTiO_3 seed crystal (MTI Corp., Richmond, CA) was placed on it. 0.5 g of packing powder was poured into the die and hand-pressed, followed by cold isostatic pressing at 50 MPa. The pressed packing powder keeps the seed crystal and pellet in close contact, which is vital for single-crystal growth. The pellet was buried with NBT-25ST atmosphere control powder in a high-purity alumina crucible with a lid and sintered in an oxygen atmosphere in a tube furnace at 1250 °C for 100 h with heating and cooling rates of 2 °C.min⁻¹. For further details see [22].

For microstructural analysis, samples are vertically sectioned, polished to a 1 μm finish as before, thermally etched, Pt-coated, and observed by scanning electron microscopy (SEM, Hitachi S-4700, Tokyo, Japan). Chemical composition of a single crystal was analyzed by electron probe microanalysis with four channels (EPMA, JEOL JXA-8530F PLUS, Tokyo, Japan). The single crystal was separated from the surrounding seed crystal and matrix grains and polished as before (without thermal etching). Wavelength-dispersive spectroscopy (WDS) analysis was carried out using an accelerating voltage of 15 kV. $\text{NaAlSi}_2\text{O}_6$, $\text{Bi}_4\text{Ge}_3\text{O}_{12}$ and SrTiO_3 were used as standards. A TAPH crystal (channel 1) was used to detect Na, a PETH crystal (channel 4) was used to detect Bi, a TAP crystal (channel 3) was used to detect Sr, and a LIFH crystal (channel 4) was used to detect Ti.

To study the structure, a single crystal sample is separated from the seed crystal and surrounding matrix grains, oriented in the $[001]_C$ direction (where subscript C means pseudocubic), and polished to a 1 μm finish with diamond suspension. The sample is analyzed by X-ray diffraction (XRD, X'Pert PRO, PANalytical, Almelo, the Netherlands) in θ - 2θ (Bragg–Brentano) configuration using $\text{CuK}\alpha$ radiation, a scan range of 10 – $90^\circ 2\theta$ and a scan speed of $3^\circ.\text{min}^{-1}$. Background removal was carried out using Match! version 3.10 (Crystal Impact, Bonn, Germany). A sample for powder XRD was also prepared by grinding a single crystal sample into powder in an agate mortar and pestle. The sample was annealed after grinding at 400°C for 1 h to remove any strains. For micro-Raman scattering, a single crystal sample oriented in the $[001]_C$ direction is removed from the matrix and polished to a 1 μm finish as before on one face. The sample is annealed at 400°C for 1 h and cooled at a rate of $1^\circ\text{C}.\text{min}^{-1}$ to remove polishing strains. Micro-Raman scattering is carried out (LabRam HR800 UV Raman microscope, Horiba Jobin–Yvon, France) at room temperature in back-scattering geometry with a 515 nm diode laser and output power of 20 mW. Resolution is $\sim 0.28\text{ cm}^{-1}$. The spectrum is corrected by the Bose–Einstein factor [63]. Peak fitting of Gaussian peaks is performed using fityk 1.3.1 peak fitting software [64].

For piezoresponse force microscopy (PFM) and electrostatic force microscopy (EFM) characterization, single crystal samples oriented in the $[001]_C$ direction are removed from the seed crystal and surrounding matrix and polished to a 0.25 μm finish with diamond suspension, followed by a final polish with colloidal silica suspension. The samples are annealed to remove any strains generated during polishing. Ferroelectric domain morphology was studied by PFM (MFP-3D, Asylum Research, CA, USA). EFM measurement of the single crystal was conducted on an XE-100 Atomic Force Microscope, (Park Systems, Suwon, Korea) with a PPP-NCSTAu cantilever probe (Nanosensors, Switzerland). The probe has a force constant of 7.4 N/m and a

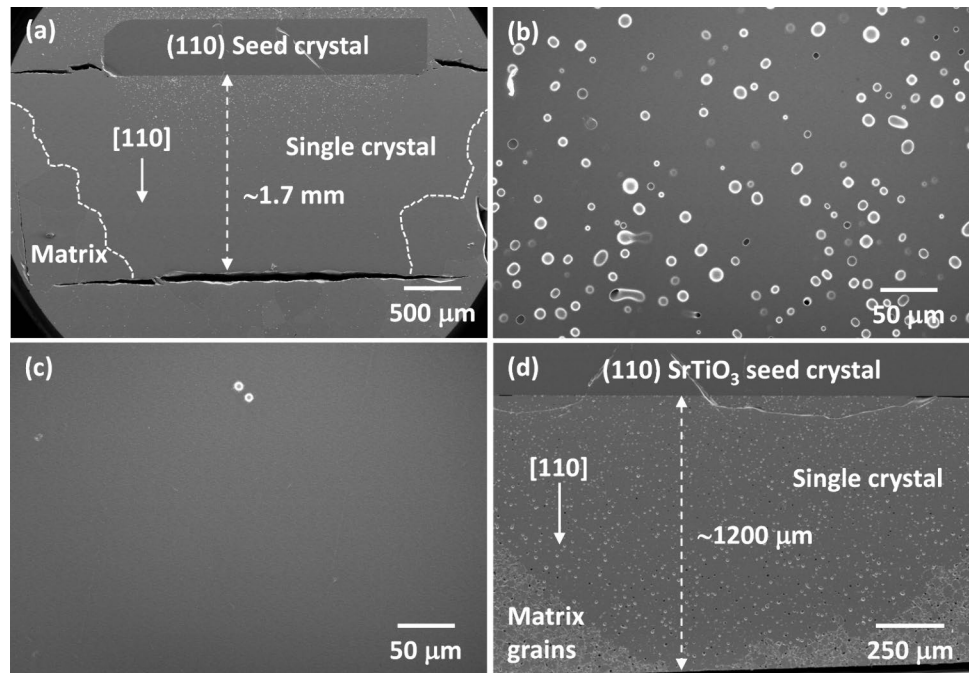
frequency of 160 kHz, with a conductive tip with a rear-side Au reflective coating. The EFM signal was enhanced by an SR 830 DSP lock-in amplifier (Stanford Research Systems, Sunnyvale, CA). All measurements were carried out in the dynamic contact EFM mode to gain a higher resolution signal with a scan rate of 0.5 Hz, scan area of $1\ \mu\text{m} \times 1\ \mu\text{m}$ or $12.5\ \mu\text{m} \times 12.5\ \mu\text{m}$, tip bias servo of 0.5 V, tip bias servo gain of 1 V, and sample bias of +10 V and –10 V during domain writing.

For impedance spectroscopy, a single crystal sample is separated from the seed crystal and surrounding matrix grains, oriented in the $[001]_C$ direction and polished with SiC paper on both major faces up to grade #4000. Both $[001]_C$ faces of the single crystal are coated with Pt-paste and the sample is annealed at 900°C for 30 min with heating and cooling rates of $5^\circ\text{C}.\text{min}^{-1}$ to prepare Pt electrodes. The sample is placed in a hot stage (TS1500, Linkam, Tadworth, UK) and the electrical properties are measured by an impedance analyzer (HP4284A, Hewlett-Packard, Kobe, Japan). Measurements were carried out in oxygen with an AC voltage of 0.1 V, a frequency range from 1000 kHz to 39.8 Hz and a temperature range of 30 – 800°C ($1^\circ\text{C}.\text{min}^{-1}$ heating and cooling rates). For measurement of polarization and strain hysteresis, two single crystal samples are prepared as above and silver paste electrodes are applied on the $[001]_C$ major faces, followed by drying in a drying oven at 100°C for 30 min. Polarization (P) and strain (S) hysteresis with external electric field (E) are measured (aixPES, aixACCT system GmbH, Aachen, Germany) using a bipolar electric field profile at 1 Hz.

3 Results and discussion

SEM micrographs of an NBT-25ST single crystal are shown in Fig. 1. Epitaxial single-crystal growth has taken place on the $[110]$ SrTiO_3 seed crystal (Fig. 1a). The white dashed lines show the single crystal/matrix grain boundary. The single crystal has grown down through the whole thickness of the pre-sintered pellet, with a growth distance of $\sim 1.7\text{ mm}$. The single crystal has also grown laterally beyond the seed crystal, as well as up into the compressed packing powder. The extent of single crystal growth is improved compared to the NBT-25ST single crystals grown in the air (Fig. 1d) [22]. The single crystal region near the seed crystal shows considerable porosity (Fig. 1b) while the region further from the seed is almost pore-free (Fig. 1c). Thus, the sample density can be considered to be much improved in the region far from the seed crystal. Sample density is also improved in this sample compared to NBT-25ST single crystals grown in air (Fig. 1d) [22]. The single crystal grown in oxygen has consumed most of the adjacent grains in the matrix and left only a few exaggerated grains several hundred microns in

Fig. 1 **a** SEM micrograph of a $0.75(\text{Na}_{0.5}\text{Bi}_{0.5})\text{TiO}_3$ - 0.25SrTiO_3 single crystal grown in oxygen at $1250\text{ }^\circ\text{C}$ for 100 h; **b** single crystal region near the seed crystal; **c** single crystal region far from the seed crystal; **d** SEM micrograph of a $0.75(\text{Na}_{1/2}\text{Bi}_{1/2})\text{TiO}_3$ - 0.25SrTiO_3 single crystal grown in air at $1250\text{ }^\circ\text{C}$ for 100 h. **d** is reproduced from [22] under the terms of the CC-BY license



diameter (Fig. 1a). These exaggerated grains are much larger than the matrix grains in the corresponding sample sintered in air (Fig. 1d) [22]. A few island grains were trapped in the single crystal bulk. These grains are believed to have low-angle grain boundaries with a single crystal [65]. Differential shrinkage between the pre-sintered pellet and the surrounding pressed packing powder during sintering has caused cracks to form at the interface between the two.

During solid-state crystal growth, the single crystal, which is essentially an abnormal grain whose formation has been deliberately induced by the seed crystal, grows by consuming the surrounding matrix grains. Any pores in the matrix may also be incorporated into the single crystal. This will happen if pores on the single crystal/matrix grain boundary cannot move quickly enough to keep up with the boundary as it moves [66, 67]. Once isolated inside the single crystal, the pressure of the gas trapped inside the pore counterbalances the capillary pressure due to pore curvature and will limit the shrinkage of the pore [68, 69]. Removal of pores trapped inside the single crystal is very difficult, as the gas trapped inside the pore must diffuse to the single crystal/matrix grain boundary in order for the pore to shrink [66]. Oxygen more readily diffuses through the lattice than nitrogen and so the NBT-25ST single crystal grown in oxygen is expected to be less porous than a crystal grown in air, as is indeed the case [22].

In the NBT-25ST single crystal grown in air, the pores were evenly distributed throughout the single crystal (Fig. 1d [22]), whereas in the NBT-25ST single crystal grown in oxygen, there is a higher concentration of pores in the region near the seed crystal (Fig. 1a, b). There could be several

reasons for this variation in porosity. As discussed above, the oxygen gas trapped in the pores can diffuse through the crystal lattice. If the pores are close to the single crystal/matrix grain boundary, the oxygen can diffuse from the pore to the boundary, allowing the pore to shrink. If the pores are too far away, then the oxygen cannot diffuse to the boundary and the pore cannot shrink. Hence pores near the single crystal/matrix grain boundary are able to shrink and disappear during sintering in oxygen. The second reason is due to the densification of the pellet that the single crystal is growing into. In single crystals grown in both air and oxygen, the NBT-25ST pellet was pre-sintered at $900\text{ }^\circ\text{C}$ for 1 h. Such a low sintering temperature was chosen to limit grain growth in the pellet, as the driving force for single crystal growth has an inverse dependence on mean matrix grain size [47, 70]. In the subsequent annealing stage at $1250\text{ }^\circ\text{C}$, the single crystal is growing into a porous matrix that is still in the process of densification. The single crystal region near the seed crystal in the single crystals grown in both air and oxygen is porous because the single crystal grew into the matrix before all the pores could be removed. In the single crystal grown in oxygen, the single crystal region farther from the seed is denser because most of the porosity in the matrix has been removed by the time the single crystal reaches it. The matrix in the sample sintered in oxygen is probably denser than the sample sintered in air, due to the increased diffusivity of oxygen.

The EPMA analysis results of an NBT-25ST single crystal are given in Table 1. Results are the mean and standard deviation of five analysis points taken across the whole sample. The O content is calculated based on the cation content.

Table 1 EPMA results of a $0.75(\text{Na}_{0.5}\text{Bi}_{0.5})\text{TiO}_3\text{-}0.25\text{SrTiO}_3$ single crystal grown in oxygen at $1250\text{ }^\circ\text{C}$ for 100 h

Element	Mean	St dev	Nominal
Na	0.340	0.008	0.375
Bi	0.382	0.002	0.375
Sr	0.249	0.003	0.25
Ti (normalized to 1 atom)	1.000	–	1

The single crystal is Na-deficient and slightly Bi-excess, while the amount of Sr is very close to the nominal value. The Na deficiency was attributed to the Na evaporation during prolonged sintering of 100 h at elevated temperatures. The slight Bi excess may form to maintain charge balance [71]. Because of the prolonged sintering, oxygen vacancies are expected to be present in the crystal structure.

An XRD pattern of a bulk NBT-25ST single crystal is shown in Fig. 2a. The peaks are indexed with the pattern for cubic $(\text{Na}_{0.5}\text{Bi}_{0.5})\text{TiO}_3$ (Crystallographic Open Database #96-210-3298, space group $\text{Pm}\bar{3}\text{m}$). For a θ - 2θ X-ray diffractometer, only crystallographic planes parallel to the surface of the sample are able to diffract X-rays [72]. The pattern shows intense 100 and 200 peaks, showing that the sample is truly a single crystal. There is a small shoulder on the low-angle side of the 100 peaks (inset in Fig. 2a). This may be caused by a surface layer on the single crystal with a different structure to the bulk crystal as found for $(\text{Na}_{0.5}\text{Bi}_{0.5})\text{TiO}_3\text{-BaTiO}_3$ [73]. The XRD pattern of a powder single crystal sample is shown in Fig. 2b, c. Rietveld refinements were carried out on this pattern using monoclinic (Cc), tetragonal (P4bm), cubic ($\text{Pm}\bar{3}\text{m}$), rhombohedral (R3c), mixed rhombohedral (R3c) + cubic ($\text{Pm}\bar{3}\text{m}$) and mixed tetragonal (I4cm) + cubic ($\text{Pm}\bar{3}\text{m}$) phases. The fitting results are shown in Table 2 and Fig. 2b, c for the mixed rhombohedral (R3c) + cubic ($\text{Pm}\bar{3}\text{m}$) phases and the mixed tetragonal (I4cm) + cubic ($\text{Pm}\bar{3}\text{m}$) phases. The combination

Table 2 Rietveld refinement fitting results of a $0.75(\text{Na}_{0.5}\text{Bi}_{0.5})\text{TiO}_3\text{-}0.25\text{SrTiO}_3$ single crystal grown in oxygen at $1250\text{ }^\circ\text{C}$ for 100 h

Phases	R_{exp}	R_{wp}	R_{p}	χ^2
R3c (94.68%) + $\text{Pm}\bar{3}\text{m}$ (5.32%)	0.02961	0.1658	0.1112	31.36
I4cm (89.81%) + $\text{Pm}\bar{3}\text{m}$ (10.19%)	0.02963	0.1281	0.0938	18.69

of a major tetragonal phase and a minor cubic phase, with space groups of I4cm and $\text{Pm}\bar{3}\text{m}$ respectively, gives the best fitting results. The lattice parameters for the tetragonal and cubic phases are given in Table 3.

$(\text{Na}_{0.5}\text{Bi}_{0.5})\text{TiO}_3$ is generally considered to have a rhombohedral (R3c) or monoclinic (Cc) structure at room temperature [74–76], although recent work has raised the possibility of a tetragonal structure [77]. The small non-cubic distortion of the unit cell [74] makes assigning a structure difficult. Previous XRD studies of polycrystalline NBT-25ST samples have assigned a trigonal [78], rhombohedral (R3c) [1], coexisting rhombohedral/ cubic or pseudocubic [22, 79, 80], coexisting tetragonal/pseudocubic [14], cubic [7, 81] or pseudocubic [2, 5, 6, 82] structure. The structure of the NBT-25ST single crystal in the present work appears to be a mixture of tetragonal and cubic phases, which differs from most of the results above. Growing the crystal in oxygen, which is expected to reduce the oxygen vacancy concentration, may be the cause for the difference in structure but more work is needed to confirm this.

The Raman spectrum of the NBT-25ST single crystal is presented in Fig. 3. The black curve is the raw data, the blue curves fitted Gaussian peaks and the red curve is the sum of the peaks. Similar to the $(\text{Na}_{0.5}\text{Bi}_{0.5})\text{TiO}_3$ structure, the Raman spectrum consists of four regions from 0 to 200 cm^{-1} , 200 to 450 cm^{-1} , 450 to 700 cm^{-1} and 700 to 900 cm^{-1} [22, 23, 83–86]. Modes between 0 and 200 cm^{-1} are assigned to Na–O, Bi–O or other A-site

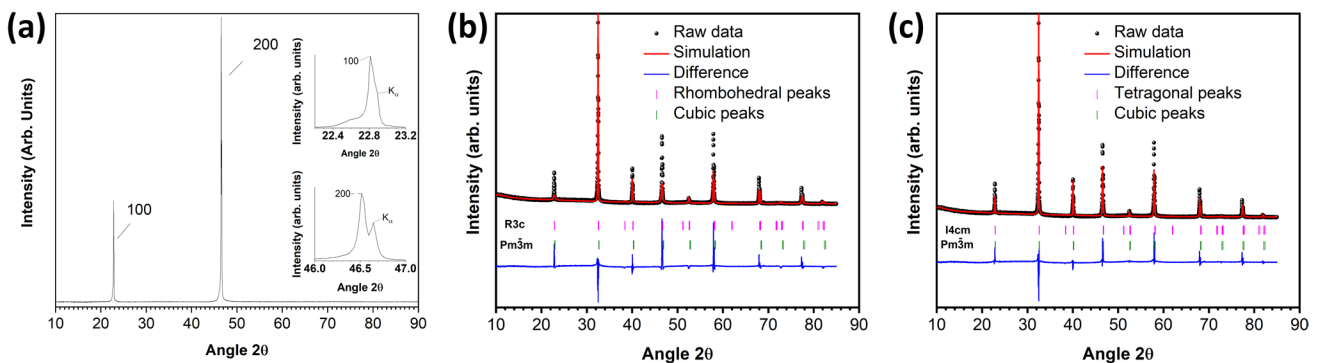
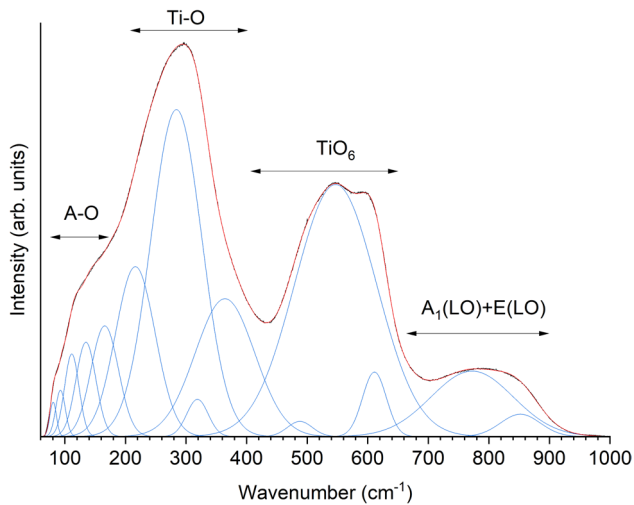
**Fig. 2** a XRD pattern of a bulk $0.75(\text{Na}_{0.5}\text{Bi}_{0.5})\text{TiO}_3\text{-}0.25\text{SrTiO}_3$ single crystal grown in oxygen at $1250\text{ }^\circ\text{C}$ for 100 h; b, c XRD patterns and Rietveld refinement of a $0.75(\text{Na}_{0.5}\text{Bi}_{0.5})\text{TiO}_3\text{-}0.25\text{SrTiO}_3$ single crystal powder sample

Table 3 Lattice parameters of tetragonal and cubic phases of a $0.75(\text{Na}_{0.5}\text{Bi}_{0.5})\text{TiO}_3\text{-}0.25\text{SrTiO}_3$ single crystal grown in oxygen at $1250\text{ }^\circ\text{C}$ for 100 h

Phase	a (Å)	b (Å)	c (Å)	α (°)	β (°)	γ (°)
Tetragonal (I4cm)	5.503516	5.503516	7.777166	90.0000	90.0000	90.0000
Cubic ($\text{Pm}\bar{3}\text{m}$)	3.891389	3.891389	3.891389	90.0000	90.0000	90.0000

**Fig. 3** Raman spectrum of a $0.75(\text{Na}_{0.5}\text{Bi}_{0.5})\text{TiO}_3\text{-}0.25\text{SrTiO}_3$ single crystal grown in oxygen at $1250\text{ }^\circ\text{C}$ for 100 h

cation-oxygen vibrations [3, 84, 87–89]. Modes between 200 and 450 cm^{-1} are assigned to Ti–O vibrations, while modes between 450 and 700 cm^{-1} are assigned to vibrations and rotations of the TiO_6 octahedra [3, 84]. Modes between 700 and 900 cm^{-1} are probably caused by overlapping bands associated with $A_1(\text{LO})$ and $E(\text{LO})$ vibrations [90]. The spectrum in Fig. 3 can be compared with the spectra of the related $(\text{Na}_{0.5}\text{Bi}_{0.5})\text{TiO}_3\text{-BaTiO}_3$ system. Raman spectra of the rhombohedral phase of $(\text{Na}_{0.5}\text{Bi}_{0.5})\text{TiO}_3\text{-BaTiO}_3$ have a narrow peak at $\sim 280\text{ cm}^{-1}$ and merged peaks between 500 and 600 cm^{-1} , whereas the tetragonal phase has a broad peak with a shoulder at $\sim 280\text{ cm}^{-1}$ and the peaks between 500 and 600 cm^{-1} are more separated [88, 91, 92]. The peak at $\sim 280\text{ cm}^{-1}$ in Fig. 3 is quite broad but has not yet developed a shoulder on the high wavenumber side, while the peaks between 500 and 600 cm^{-1} are beginning to separate. This indicates that the NBT-25ST single crystal is at the morphotropic phase boundary between the rhombohedral and tetragonal phases. The Rietveld refinement of the powder XRD pattern indicates that the single crystal contains tetragonal and cubic phases, whereas the Raman scattering results indicate the single crystal contains rhombohedral and tetragonal phases. Ferroelectric materials often have different structures at different length scales [77, 92–94].

Piezoresponse force microscopy (PFM) is based on atomic force microscopy but uses a conductive tip. An alternating voltage is applied to the tip as the sample is scanned across a ferroelectric material in contact mode. A strain develops in the material due to the converse piezoelectric effect, which causes displacement of the tip. The amplitude of the displacement is proportional to the induced strain while the phase difference between the applied alternating voltage and the tip vibration frequency is related to domain polarization orientation [95, 96]. PFM can be used to image ferroelectric domains and to study domain switching. PFM images of two regions ($30\text{ }\mu\text{m} \times 30\text{ }\mu\text{m}$ and $20\text{ }\mu\text{m} \times 20\text{ }\mu\text{m}$) of an NBT-25ST single crystal are shown in Fig. 4. No features can be detected in the amplitude (Fig. 4b, e) and phase (Fig. 4c, f) diagrams. It is clear that no piezoresponse was measured in either region and hence no ferroelectric domains are present in the single crystal [15, 97, 98]. Electrostatic force microscopy (EFM) is another variation of atomic force microscopy which is used to image both surface topography and regions of different surface potential or charge by detecting the electrostatic force between the sample surface and the tip when a dc and ac bias are applied between the two [99–101]. Analogous to PFM, EFM can be used to image as well as switch ferroelectric domains [99, 100, 102–105]. EFM images of a $1\text{ }\mu\text{m} \times 1\text{ }\mu\text{m}$ region of an NBT-25ST single crystal are shown in Fig. 5a–c. Similar to the PFM images, no features are visible in the amplitude (Fig. 5b) and phase (Fig. 5c) diagrams and hence no ferroelectric domains are detected. To assess the possibility of inducing polarization, a rectangular shape ($4.5\text{ }\mu\text{m} \times 4.1\text{ }\mu\text{m}$) was drawn on the surface of the sample with a tip voltage of -10 V (Fig. 5d, e), while the surrounding area was drawn with a tip voltage of $+10\text{ V}$. The edge of the sample, marked 0 V , was drawn without a bias voltage. After that, the area was scanned and the amplitude and phase images are shown in Fig. 5d, e respectively. It can be seen that a ferroelectric domain has been written into the sample surface [96–98, 105]. The absence of ferroelectric domains as shown by the PFM and EFM measurements of the as-prepared sample (Figs. 4 and 5a–c) indicate that the NBT-25ST single crystal is in an ergodic relaxor state [15, 97, 98, 106]. Figure 5e, f show that it is possible to form a stable ferroelectric domain by applying a sufficient bias voltage [96–98, 105], implying that NBT-25ST can undergo an electric-field induced transition from the relaxor to the ferroelectric state. Similar

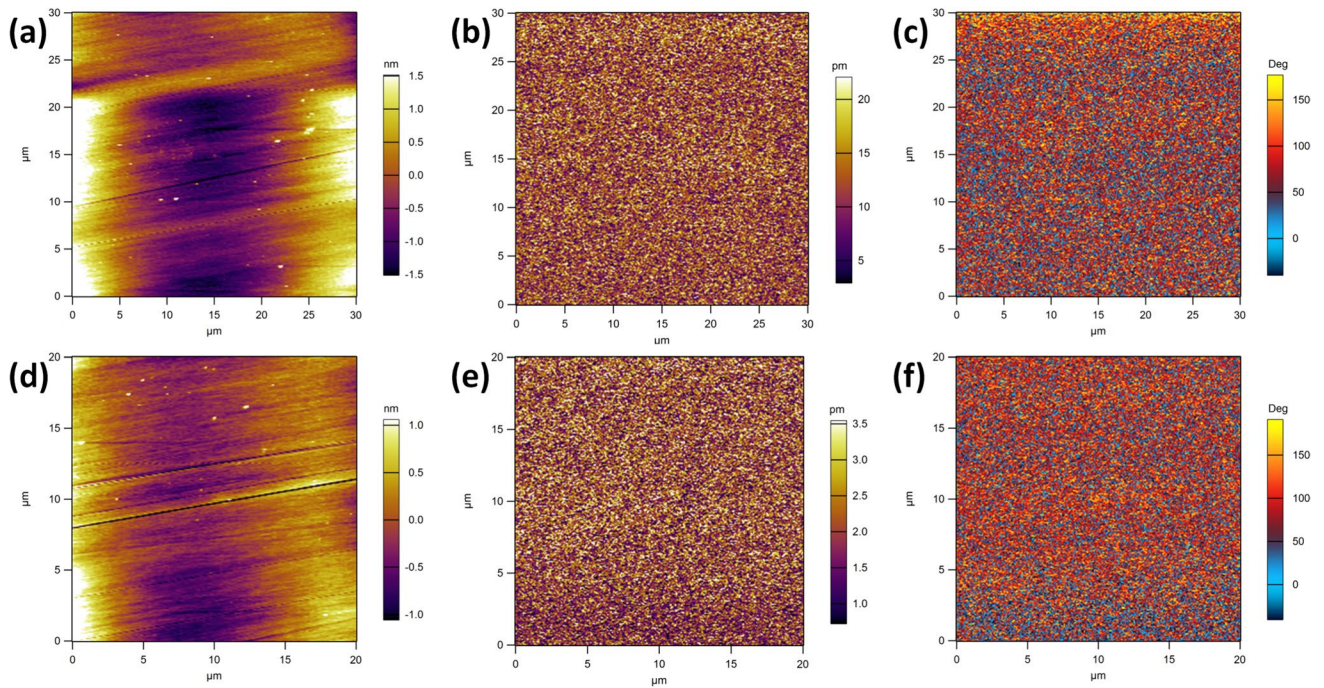


Fig. 4 PFM images of a $0.75(\text{Na}_{0.5}\text{Bi}_{0.5})\text{TiO}_3\text{-}0.25\text{SrTiO}_3$ single crystal grown in oxygen at $1250\text{ }^\circ\text{C}$ for 100 h: **a, d** topography; **b, e** amplitude; **c, f** phase

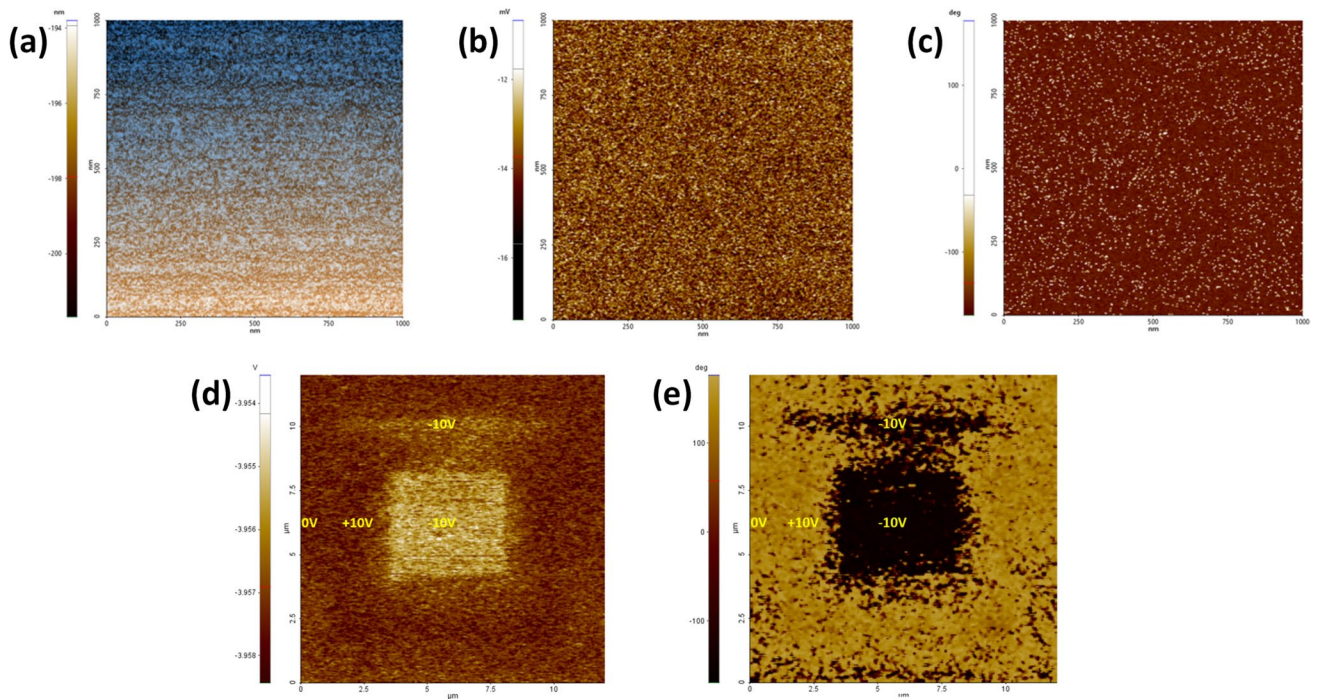


Fig. 5 EFM images of a $0.75(\text{Na}_{0.5}\text{Bi}_{0.5})\text{TiO}_3\text{-}0.25\text{SrTiO}_3$ single crystal grown in oxygen at $1250\text{ }^\circ\text{C}$ for 100 h: **a** topography; **b** amplitude; **c** phase; **e** amplitude and **f** phase of a region after domain writing

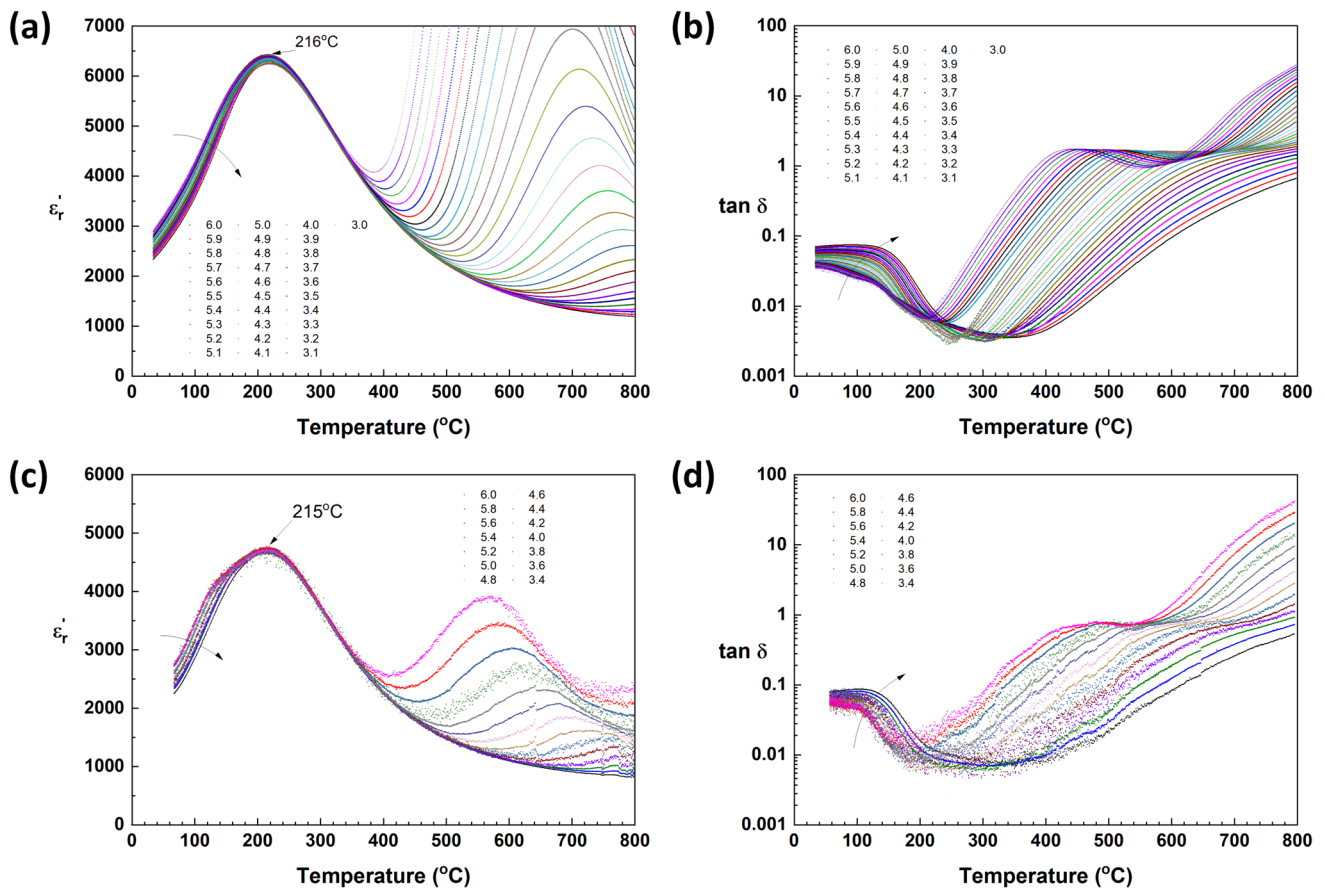


Fig. 6 **a** Relative permittivity vs. temperature; **b** loss tangent vs. temperature of a $0.75(\text{Na}_{0.5}\text{Bi}_{0.5})\text{TiO}_3\text{-}0.25\text{SrTiO}_3$ single crystal grown in oxygen at $1250\text{ }^\circ\text{C}$ for 100 h; **c** relative permittivity vs. temperature;

d loss tangent vs. temperature of a $0.75(\text{Na}_{0.5}\text{Bi}_{0.5})\text{TiO}_3\text{-}0.25\text{SrTiO}_3$ single crystal grown in air at $1250\text{ }^\circ\text{C}$ for 100 h. **c** and **d** are reproduced from [22] under the terms of the CC-BY license

behaviour is seen in other NBT-based materials [18, 87, 97, 98].

Figure 6a and b shows the relative permittivity and loss tangent plots on cooling of an NBT-25ST single crystal grown in oxygen. Numbers in the legend are the logarithm (base 10) of the measurement frequency. The arrows indicate increasing measurement frequency. Frequency dispersion is seen in the relative permittivity vs. temperature curves. The shoulder commonly seen at lower temperatures in NBT-based materials [8, 22, 35, 39, 40, 46] is not visible during either heating or cooling. The temperature of maximum permittivity T_m is at $\sim 216\text{ }^\circ\text{C}$ with a slight frequency dispersion. Hysteresis in the temperature of maximum permittivity T_m is limited to $4\text{ }^\circ\text{C}$ at 10^6 Hz ($223\text{ }^\circ\text{C}$ and $219\text{ }^\circ\text{C}$ for heating and cooling respectively). The increase in relative permittivity and the large dispersion at temperatures above $350\text{ }^\circ\text{C}$ is caused by conduction effects [77] or polarisation effects at the electrodes. The loss tangent curves show a shoulder at low temperatures which is commonly seen in NBT-based materials [2, 3, 8, 18, 22, 28, 77]. The plateau in loss tangent at temperatures $> 400\text{ }^\circ\text{C}$ appears to be connected to the

conduction or polarisation effects. For comparison, Fig. 6c, d shows the relative permittivity and loss tangent plots of an NBT-25ST single crystal grown in air [22]. The value of T_m is similar to that of the single crystal grown in oxygen while the high-temperature conduction/polarisation effects are less pronounced. The shoulder in the loss tangent curves also appears at a similar temperature to that of the single crystal grown in oxygen, while the high-temperature plateau is at lower values of loss tangent. NBT-ST ceramics of similar composition in the literature have values of T_m between 170 and $215\text{ }^\circ\text{C}$ [1, 2, 5, 7, 8, 14, 22, 28]. The value of T_m in the NBT-25ST single crystals grown both in air and in oxygen is at the higher end of these values.

The absence of the low-temperature shoulder from the relative permittivity vs. temperature plots in Fig. 6a is unusual, as it is present in the relative permittivity vs. temperature plots of the NBT-25ST single crystal grown in air (Fig. 6c) [22]. The existence of this low-temperature shoulder has been ascribed to several reasons: a transition between rhombohedral and mixed rhombohedral/tetragonal phases [8, 107–110], a transition between rhombohedral and

mixed rhombohedral/orthorhombic phases [111], thermal evolution of mixed rhombohedral/tetragonal polar nanoregions [112], thermal activation of polar nanoregions [113] or a non-ergodic to ergodic relaxor transition [114]. Liu et al. studied the effect of grain size on the dielectric properties of NBT-26ST ceramics sintered in air [18]. They found that an increase in grain size made the shoulder more pronounced and reduced frequency dispersion at temperatures above the shoulder, which they attributed to a reduction in internal stresses. However, the NBT-25ST single crystal in the present study shows no low-temperature shoulder and shows frequency dispersion even above T_m . From the XRD results, the long-range order of the single crystal appears to be a mixture of tetragonal and cubic phases. From the Raman scattering results, the single crystal appears to consist of mixed rhombohedral and tetragonal phases at the unit cell scale. Therefore, on heating, the rhombohedral-tetragonal transition may be less pronounced, explaining the absence

of the shoulder. A corresponding shoulder is still present in the $\tan \delta$ vs. temperature plot in Fig. 6b.

Two single crystal samples were prepared for polarization and strain hysteresis measurements. For the second sample, the porous layer that was originally adjacent to the seed crystal (similar to that in Fig. 1a) was removed by polishing, whereas it was not removed from the first sample. Polarization–electric field (PE) and bipolar strain–electric field (SE) hysteresis loops of the first sample were measured as shown in Fig. 7. The maximum electric field that could be applied to this sample was 3 kV/mm. The pinched PE hysteresis loops (Fig. 7a) and sprout-shaped SE loops with almost zero remanent and negative strain (Fig. 7b) indicate that the sample is undergoing an electric field-induced phase transition between ergodic and non-ergodic relaxor phases [4]. Compared to the NBT-25ST single crystal grown in air [22], the NBT-25ST single crystal grown in oxygen has a higher value of saturation polarization P_s at an electric field

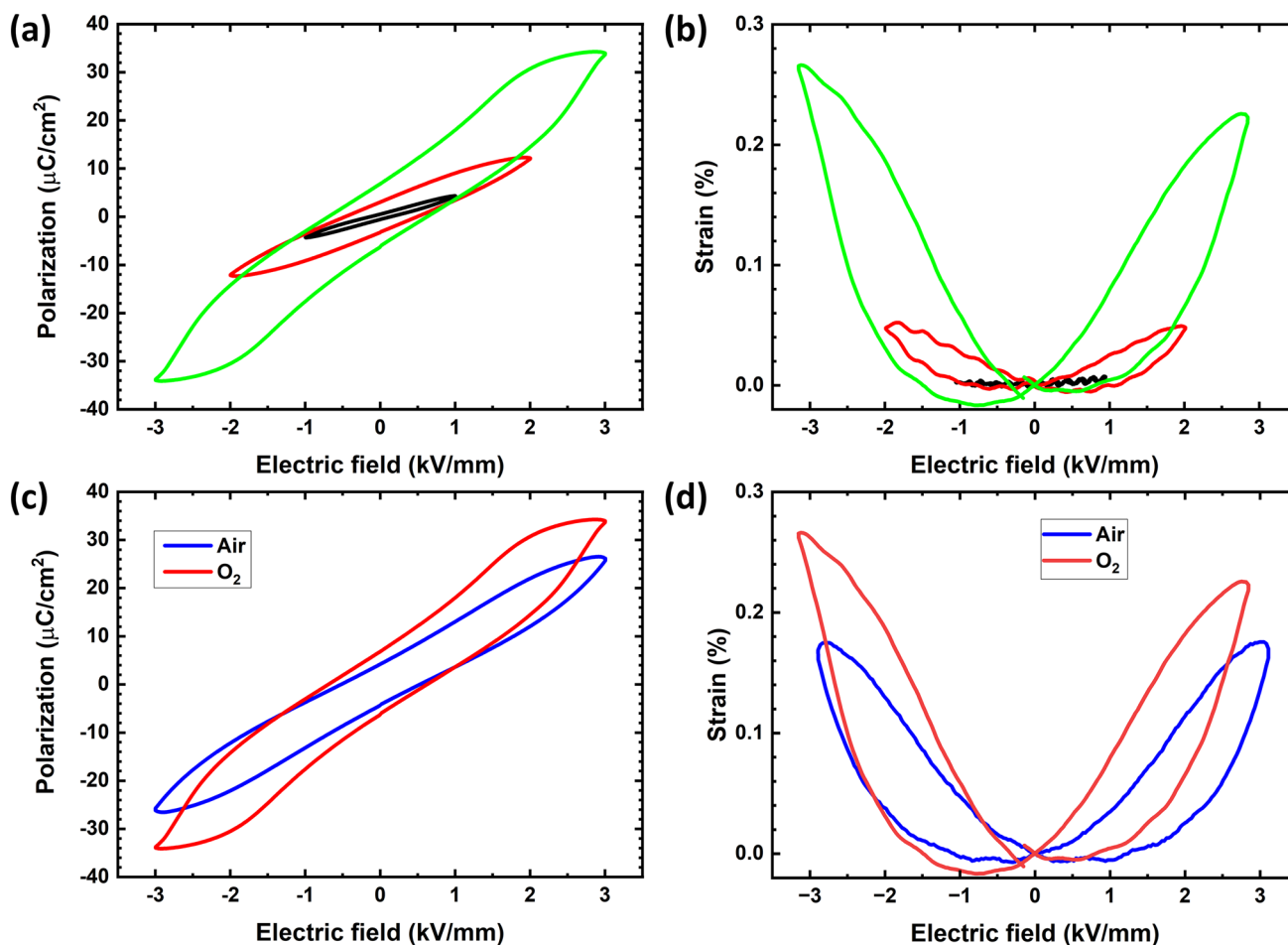


Fig. 7 **a** Polarization vs. electric field hysteresis loop; **b** strain vs. electric field hysteresis loop of a $0.75(\text{Na}_{0.5}\text{Bi}_{0.5})\text{TiO}_3-0.25\text{SrTiO}_3$ single crystal grown in oxygen at 1250°C for 100 h. **c**, **d** Comparison of the **c** polarization vs. electric field and **d** strain vs. electric field

hysteresis loops of $0.75(\text{Na}_{0.5}\text{Bi}_{0.5})\text{TiO}_3-0.25\text{SrTiO}_3$ single crystals grown in oxygen and in air at 1250°C for 100 h. PE and SE hysteresis loops of the single crystal grown in the air are reproduced from [22] under the terms of the CC-BY license

Table 4 Ferroelectric and piezoelectric properties of $0.75(\text{Na}_{0.5}\text{Bi}_{0.5})\text{TiO}_3\text{-}0.25\text{SrTiO}_3$ single crystals grown in oxygen and air at 1250 °C for 100 h

Sintering atmosphere	E_{max} (kV/mm)	P_r ($\mu\text{C}/\text{cm}^2$)	P_s ($\mu\text{C}/\text{cm}^2$)	E_c (kV/mm)	S_{max} (%)	$S_{\text{max}}/E_{\text{max}}$ (pm/V)	$\Delta S/S_{\text{max}}$ (%)	References
Oxygen	3.0	6.8	34.3	0.69	0.22	784	47.2	This work
Air	3.0	4.2	26.5	0.52	0.17	546	40.2	[22]

of 3 kV/mm and slightly larger values of remanent polarization P_r and coercivity E_c (Fig. 7c and Table 4). Both single crystals grown in air and oxygen have sprout-shaped hysteresis loops, but the single crystal grown in oxygen has higher values of S_{max} and $S_{\text{max}}/E_{\text{max}}$ (Fig. 7d and Table 4). $S_{\text{max}}/E_{\text{max}}$ in the single crystal grown in oxygen is improved by 44% compared to the single crystal grown in air and by 99% compared to a NBT-25ST ceramic sample sintered in air [22]. However, strain hysteresis ($\Delta S/S_{\text{max}}$, where ΔS is

the difference between the upper and lower parts of the loop when $E = E_{\text{max}}/2$ [115]) was increased in the single crystal grown in oxygen, becoming comparable to that of the ceramic sample sintered in air.

Polarization–electric field (PE) and bipolar strain–electric field (SE) hysteresis loops of the second sample were measured as shown in Fig. 8. The maximum electric field that could be applied to this sample was 3.5 kV/mm. Again, the sample has pinched PE hysteresis

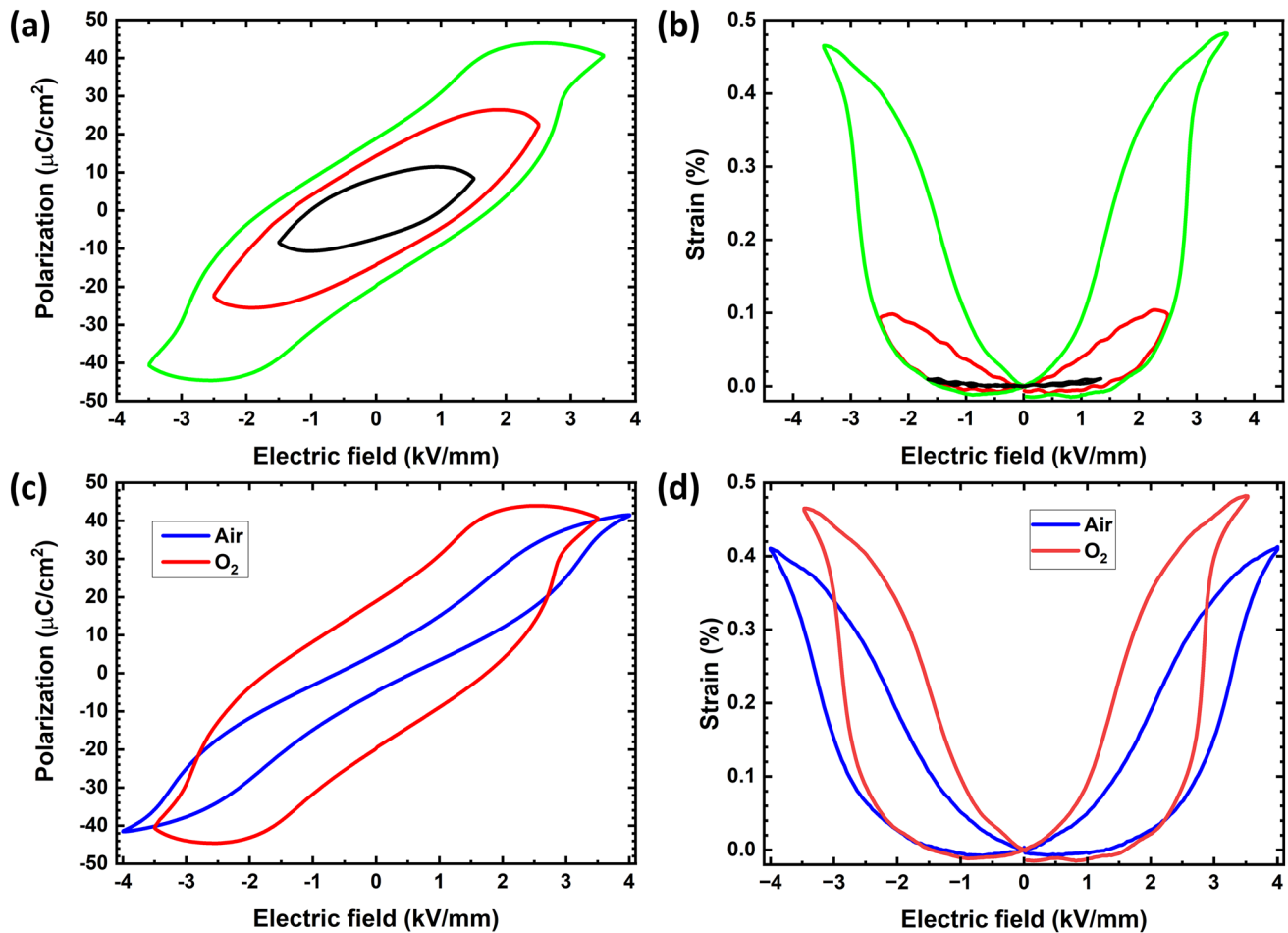
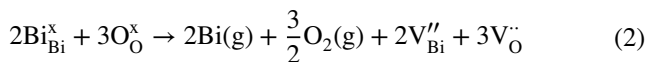
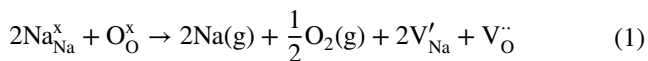


Fig. 8 **a** Polarization vs. electric field hysteresis loop; **b** strain vs. electric field hysteresis loop of the second $0.75(\text{Na}_{0.5}\text{Bi}_{0.5})\text{TiO}_3\text{-}0.25\text{SrTiO}_3$ single crystal grown in oxygen at 1250 °C for 100 h. **c**, **d** Comparison of the **c** polarization vs. electric field and **d** strain vs.

electric field hysteresis loops of $0.75(\text{Na}_{0.5}\text{Bi}_{0.5})\text{TiO}_3\text{-}0.25\text{SrTiO}_3$ single crystals grown in oxygen and in air at 1250 °C for 100 h. PE and SE hysteresis loops of the single crystal grown in the air are reproduced from [22] under the terms of the CC-BY license

loops (Fig. 8a) and sprout-shaped SE loops with nearly zero remanent and negative strain (Fig. 8b). However, the PE loops look very different from those of the first sample. The loops in the second sample have opened out with much larger values of P_r and E_c . Compared to the NBT-25ST single crystal grown in air and measured at an electric field of 4 kV/mm [22], the second sample of the NBT-25ST single crystal grown in oxygen has similar values of P_s , but considerably larger values of P_r and E_c (Fig. 8c and Table 5). Both single crystals grown in air and oxygen have sprout-shaped SE hysteresis loops, but the single crystal grown in oxygen has higher values of S_{\max} and S_{\max}/E_{\max} (Fig. 8d and Table 5). S_{\max}/E_{\max} in the single crystal grown in oxygen is improved by 32% compared to the single crystal grown in air and by 97% compared to a NBT-25ST ceramic sample sintered in air [22]. However, strain hysteresis was increased in the single crystal grown in oxygen, becoming comparable to that of the ceramic sample sintered in air. S_{\max}/E_{\max} is also improved compared to the first sample grown in oxygen.

During crystal growth, Na and Bi can evaporate according to the following reactions [61, 116]:



During cooling from 1000 °C to 600 °C, the oxygen vacancies can be removed by the following reaction [62]:



Growth of single crystals of NBT and NBT-BaTiO₃ in an oxygen atmosphere suppressed their leakage current, indicating a reduced concentration of oxygen vacancies in the crystals by suppression of defect reactions (1) and (2) [59, 61]. Thermogravimetric analysis of La-doped NBT powders also showed that an increase of oxygen partial pressure in the measurement atmosphere reduced weight losses, showing suppression of the defect reactions (1) and (2) [59]. Growth of NBT-25ST single crystals in an oxygen atmosphere can likewise suppress defect reactions (1) and

(2) and promote defect reaction (3), leading to a reduction in oxygen vacancies in the single crystal.

From Fig. 7a, the PE loops of the first NBT-25ST single crystal sample grown in oxygen begin to saturate at an electric field of 2 kV/mm. The single crystal grown in oxygen has higher values of P_s and P_r than the single crystal grown in air (Fig. 7c and Table 4). Oxygen vacancies are known to inhibit domain wall movement [117–121] as well as the rotation of non-180° domains [59, 61, 122, 123]. The higher values of P_s and P_r indicate that a reduction in oxygen vacancies promotes the growth of ferroelectric domains, promotes domain rotation to align with the electric field and suppresses domain clamping [59, 62, 124, 125].

From Fig. 8a, the PE loops of the second NBT-25ST single crystal sample grown in oxygen begin to saturate at an electric field of 2.5 kV/mm. The slope of the polarization vs. electric field curve with a maximum electric field of 3.5 kV/mm increases rapidly above this point, while in the curve for the single crystal grown in air, the slope begins to rise rapidly at electric fields > 3 kV/mm (Fig. 8c). The slope is also steeper in the single crystal grown in oxygen. This indicates that the relaxor-ferroelectric phase transition begins at lower electric fields and that the growth of ferroelectric domains is enhanced in the single crystal grown in oxygen. Comparing the strain vs. electric field curves in Fig. 8d, the strain begins to increase noticeably in single crystals grown both in air and in oxygen at an electric field of 1.5 kV/mm. After this point, strain increases more rapidly with an electric field for the single crystal grown in oxygen, again indicating that a reduction in oxygen vacancies promotes the growth and rotation of ferroelectric domains.

The curvature at the top and bottom of the hysteresis loops of the second NBT-25ST single crystal sample grown in oxygen (between $E = 1.5 \sim 3.5$ kV/mm and $-1.5 \sim -3.5$ kV/mm) (Fig. 8a, d) indicate increased conductivity in the single crystal compared to the first sample grown in oxygen and the single crystal grown in air [126]. This increase in conductivity may also explain the increased P_r and E_c of the second single crystal sample grown in oxygen [126]. This behaviour is unexpected, as growing the single crystal in oxygen should suppress defect reactions (1) and (2) as discussed above, leading to a reduction in leakage current. Growth of the single crystal in oxygen promotes defect reaction (3) as the crystal cools down, leading to an increase in

Table 5 Ferroelectric and piezoelectric properties of 0.75(Na_{0.5}Bi_{0.5})TiO₃-0.25SrTiO₃ single crystals grown in oxygen and air at 1250 °C for 100 h

Sintering atmosphere	E_{\max} (kV/mm)	P_r ($\mu\text{C}/\text{cm}^2$)	P_s ($\mu\text{C}/\text{cm}^2$)	E_c (kV/mm)	S_{\max} (%)	S_{\max}/E_{\max} (pm/V)	$\Delta S/S_{\max}$ (%)	References
Oxygen	3.5	18.9	40.7	1.72	0.48	1365	60.7	This work
Air	4.0	5.1	41.5	0.61	0.41	1031	39.2	[22]

electron hole concentration and increased conductivity [59, 61]. But why this happened in only one sample grown in oxygen is unknown. Doping with a donor dopant such as Nb may reduce the conductivity by removing oxygen vacancies generated by reaction (2) [127]. Changing the atmosphere to air during cooling may also reduce the conductivity by suppressing reaction (3).

4 Conclusions

Single crystals of $0.75(\text{Na}_{0.5}\text{Bi}_{0.5})\text{TiO}_3\text{-}0.25\text{SrTiO}_3$ have been grown by the top-seeded solid state crystal growth technique in an oxygen atmosphere. Single crystals grown in oxygen had improved size and density compared to crystals grown under equivalent conditions in air. Improved density is due to the easier diffusion of oxygen through the crystal lattice, allowing for pore shrinkage, as well as reduced porosity in the matrix in general. X-ray diffraction shows the long-range order of the crystal to be a mixture of tetragonal and cubic phases, while Raman scattering indicates the presence of rhombohedral and tetragonal phases at the unit cell level. Piezoresponse force microscopy and electrostatic force microscopy show that the single crystal is in the ergodic relaxor state, while electrostatic force microscopy shows that ferroelectric domains can be induced by an electric field. The single crystal undergoes a reversible electric field induced relaxor to ferroelectric phase transition, with improved values of maximum strain and $S_{\text{max}}/E_{\text{max}}$ compared to single crystals grown in air ($S_{\text{max}}/E_{\text{max}} = 1365 \text{ pm/V}$ at an electric field of 3.5 kV/mm compared to 1031 pm/V at an electric field of 4 kV/mm for a single crystal grown in air). The PE hysteresis loops of two single crystals grown in oxygen are quite different from each other, with the second sample appearing to have increased conductivity, for reasons that are not yet known. Single crystals of NBT-25ST grown in oxygen have potential for use as actuators but further work needs to be carried out to confirm reproducibility of properties and reduce conductivity further.

Acknowledgements This study was financially supported by the Basic Science Research Program through the National Research Foundation of Korea (NRF), funded by the Ministry of Education under Grant number 2018R1D1A1B07041485, and by a National Research Foundation of Korea (NRF) grant funded by the Ministry of Science and ICT (MSIT) (Grant no. NRF-2018R1A5A1025224). The authors would like to thank Thi Lan Tran for assistance in measuring the dielectric properties. The authors would like to thank Hey-Jeong Kim (Centre for Development of Fine Chemicals, Chonnam National University) for operating the SEM, Dr. Sang-Hun Jeong (Korea Basic Science Institute, Gwangju center) for operating the Raman spectrometer and Kyeong-Kap Jeong and Jung-Yeol Park (Center for Research Facilities, Chonnam National University) for operating the XRD and EPMA respectively. JGF would like to thank Jurij Koruza (Graz University of Technology) for the suggestion to grow $0.75(\text{Na}_{0.5}\text{Bi}_{0.5})\text{TiO}_3\text{-}0.25\text{SrTiO}_3$ single crystals in oxygen.

Data availability The data presented in this study are available on request from the corresponding author.

Declarations

Conflict of interest The authors have no relevant financial or non-financial interests to disclose.

References

1. Y. Hiruma, Y. Imai, Y. Watanabe, H. Nagata, T. Takenaka, Appl. Phys. Lett. **92**, 262904 (2008)
2. W. Krauss, D. Schütz, F.A. Mautner, A. Feteira, K. Reichmann, J. Eur. Ceram. Soc. **30**, 1827 (2010)
3. D. Rout, K.S. Moon, S.J.L. Kang, I.W. Kim, J. Appl. Phys. **108**, 084102 (2010)
4. W. Jo, R. Dittmer, M. Acosta, J. Zang, C. Groh, E. Sapper, K. Wang, J. Rödel, J. Electroceram. **29**, 71 (2012)
5. M. Acosta, W. Jo, J. Rödel, J. Am. Ceram. Soc. **97**, 1937 (2014)
6. S. Jo, C.H. Hong, D.S. Kim, H.W. Kang, C.W. Ahn, H.G. Lee, S. Nahm, W. Jo, S.H. Han, Sens. Actuators A **258**, 201 (2017)
7. T.A. Duong, H.S. Han, Y.H. Hong, Y.-S. Park, H.T.K. Nguyen, T.H. Dinh, J.S. Lee, J. Electroceram. **41**, 73 (2018)
8. G. Liu, J. Dong, L. Zhang, Y. Yan, R. Jing, L. Jin, J. Materiomics **6**, 677 (2020)
9. J. Rödel, W. Jo, K.T.P. Seifert, E.M. Anton, T. Granzow, D. Damjanovic, J. Am. Ceram. Soc. **92**, 1153 (2009)
10. J. Rödel, K.G. Webber, R. Dittmer, W. Jo, M. Kimura, D. Damjanovic, J. Eur. Ceram. Soc. **35**, 1659 (2015)
11. J. Wu Advances in Lead-Free Piezoelectric Materials. (Springer Nature Singapore Pte Ltd., Singapore, 2018), pp. 191–246
12. A.J. Bell, O. Deubzer, MRS Bull. **43**, 581 (2018)
13. T. Takenaka, H. Nagata, in Lead-Free Piezoelectrics, ed by S. Priya, S. Nahm (Springer Science+Business Media, New York, 2012), p. 255
14. X.Y. Tong, J.J. Zhou, K. Wang, H. Liu, J.Z. Fang, J. Eur. Ceram. Soc. **37**, 4617 (2017)
15. X. Liu, B. Shen, J. Zhai, J. Am. Ceram. Soc. **102**, 6751 (2019)
16. L. Molina-Luna, S. Wang, Y. Pivak, A. Zintler, H.H. Pérez-Garza, R.G. Spruit, Q. Xu, M. Yi, B.-X. Xu, M. Acosta, Nat. Commun. **9**, 4445 (2018)
17. J. Koruza, V. Rojas, L. Molina-Luna, U. Kunz, M. Duerrschnebel, H.J. Kleebe, M. Acosta, J. Eur. Ceram. Soc. **36**, 1009 (2016)
18. X. Liu, S. Xue, F. Wang, J. Zhai, B. Shen, Acta Mater. **164**, 12 (2019)
19. K.S. Yang, M.J. Choi, J.S. Choi, J.H. Eom, B.J. Park, S.Y. Lee, S.G. Yoon, Sens. Actuators, A **243**, 117 (2016)
20. H.Y. Lee, W. Sun, J. Luo, Z. Zhou, J.F. Li, Ceram. Int. **44**, 4114 (2018)
21. P.G. Le, G.Y. Jo, S.Y. Ko, J.G. Fisher, J. Electroceram. **40**, 122 (2018)
22. P.G. Le, T.L. Pham, D.T. Nguyen, J.S. Lee, J.G. Fisher, H.P. Kim, W. Jo, Journal of Asian Ceramic Societies **9**, 40 (2021)
23. P.G. Le, T.L. Tran, H.P. Kim, W. Jo, J.S. Lee, J.G. Fisher, Open Ceram., 100099 (2021)
24. J.H. Cho, J.S. Park, S.W. Kim, Y.H. Jeong, J.S. Yun, W.I. Park, Y.W. Hong, J.H. Paik, J. Eur. Ceram. Soc. **37**, 3313 (2017)
25. F. Wang, M. Xu, Y. Tang, T. Wang, W. Shi, C.M. Leung, J. Am. Ceram. Soc. **95**, 1955 (2012)
26. M. Acosta, L.A. Schmitt, L. Molina-Luna, M.C. Scherrer, M. Brilz, K.G. Webber, M. Deluca, H.J. Kleebe, J. Rödel, W. Donner, J. Am. Ceram. Soc. **98**, 3405 (2015)

27. T. Fromling, S. Steiner, A. Ayrikyan, D. Breamecker, M. Durrschnabel, L. Molina-Luna, H.-J. Kleebe, H. Hutter, K.G. Webber, M. Acosta, *J. Mater. Chem. C* **6**, 738 (2018)
28. X. Zhou, H. Yang, G. Xue, H. Luo, D. Zhang, *J. Adv. Ceram.* **11**, 1542 (2022)
29. W. Ge, H. Liu, X. Zhao, X. Li, X. Pan, D. Lin, H. Xu, X. Jiang, H. Luo, *Appl. Phys. A* **95**, 761 (2009)
30. C. Chen, X. Jiang, Y. Li, F. Wang, Q. Zhang, H. Luo, *J. Appl. Phys.* **108**, 124106 (2010)
31. G. Cheng, H. Xia, J. Hu, Y. Zhu, B. Chen, *Mater. Res. Express* **5**, 066201 (2018)
32. A. Volpi, K.W. Krämer, D. Biner, B. Wiggins, J. Kock, A.R. Albrecht, E.J. Peterson, M.N. Spilde, M. Sheik-Bahae, M.P. Hehlen, *Cryst. Growth Des.* **21**, 2142 (2021)
33. J. Chen, X. Zhao, H. Zhang, X. Li, H. Deng, C. Chen, B. Ren, H. Luo, *Ceram. Int.* **41**, 6722 (2015)
34. K. Chen, G. Xu, D. Yang, X. Wang, J. Li, *J. Appl. Phys.* **101**, 044103 (2007)
35. Y. Wang, C. Luo, S. Wang, C. Chen, G. Yuan, H. Luo, D. Viehland, *Adv. Electron. Mater.* **6**, 1900949 (2020)
36. C. Chen, X. Zhao, Y. Wang, H. Zhang, H. Deng, X. Li, X. Jiang, X. Jiang, H. Luo, *Appl. Phys. Lett.* **108**, 022903 (2016)
37. J. Chen, H. Yan, A. Kuwabara, M.D. Smith, Y. Iwasa, H. Ogino, Y. Matsushita, Y. Tsujimoto, K. Yamaura, H.C. Zur Loye, *Front. Chem.* **8**, 91 (2020)
38. S. Zhang, M. Li, Y. Yang, C. Zhao, M. He, Y. Hang, Y. Fang, *CrystEngComm* **23**, 5045 (2021)
39. S. Bhandari, B. Kumar, *Cryst. Growth Des.* **15**, 867 (2015)
40. P.G. Le, H.T. Tran, J.S. Lee, J.G. Fisher, H.P. Kim, W. Jo, W.J. Moon, *J. Adv. Ceram.* **10**, 973 (2021)
41. S.Y. Ko, J.H. Park, I.W. Kim, S.S. Won, S.Y. Chung, S.J.L. Kang, *J. Eur. Ceram. Soc.* **37**, 407 (2017)
42. K.S. Moon, D. Rout, H.Y. Lee, S.J.L. Kang, *J. Cryst. Growth* **317**, 28 (2011)
43. H. Sun, J.G. Fisher, S.H. Moon, H. Tran Tran, J.S. Lee, H.S. Han, H.P. Kim, W. Jo, *Materials Science and Engineering: B* **223**, 109 (2017)
44. E. Uwiragiye, M.U. Farooq, S.H. Moon, T.L. Pham, D.T. Nguyen, J.S. Lee, J.G. Fisher, *J. Eur. Ceram. Soc.* **37**, 4597 (2017)
45. I. Fujii, S. Ueno, S. Wada, *J. Eur. Ceram. Soc.* **40**, 2970 (2020)
46. D. Lee, H. Vu, H. Sun, T.L. Pham, D.T. Nguyen, J.S. Lee, J.G. Fisher, *Ceram. Int.* **42**, 18894 (2016)
47. S.J.L. Kang, J.H. Park, S.Y. Ko, H.Y. Lee, *J. Am. Ceram. Soc.* **98**, 347 (2015)
48. A. Benčan, E. Tchernychova, H. Uršič, M. Kosec, J. Fisher, in *Ferroelectrics-Material Aspects*, ed by M. Lallart (InTech, Rijeka, 2011), p. 87
49. J.J. Choi, J. Ryu, H.E. Kim, *J. Am. Ceram. Soc.* **84**, 1465 (2001)
50. G.S. Snow, *J. Am. Ceram. Soc.* **56**, 91 (1973)
51. M. Spreitzer, A. Meden, D. Suvorov, *J. Eur. Ceram. Soc.* **38**, 1399 (2018)
52. X. Liu, R. Rao, J. Shi, J. He, Y. Zhao, J. Liu, H. Du, *J. Alloys Compd.* **875**, 159999 (2021)
53. M. Li, M.J. Pietrowski, R.A. De Souza, H.R. Zhang, I.M. Reaney, S.N. Cook, J.A. Kilner, D.C. Sinclair, *Nat. Mater.* **13**, 31 (2014)
54. R. Bhattacharyya, S. Omar, *Solid State Ionics* **317**, 115 (2018)
55. T.V. Kruzina, V.M. Sidak, M.P. Trubitsyn, S.A. Popov, A.Y.S.J. Tulik, *Acta Phys. Pol., A* **133**, 816 (2018)
56. J.C.C.A. Diaz, J.-C. M'Peko, M. Venet, P.S. da Silva, *Sci. Rep.* **10**, 19491 (2020)
57. V.M. Sidak, M.P. Trubitsyn, *J. Phys. Electron.* **28**, 87 (2020)
58. V.M. Sidak, M.P. Trubitsyn, T.V. Panchenko, *Condens. Matter Phys.* **25**, (2022)
59. K. Yamamoto, M. Suzuki, Y. Noguchi, M. Miyayama, *Jpn J Appl Phy* **47**, 7623 (2008)
60. K. Makisumi, Y. Kitanaka, Y. Noguchi, M. Miyayama, *J. Ceram. Soc. Jpn.* **125**, 463 (2017)
61. Y. Noguchi, I. Tanabe, M. Suzuki, M. Miyayama, *J. Ceram. Soc. Jpn.* **116**, 994 (2008)
62. H. Onozuka, Y. Kitanaka, Y. Noguchi, M. Miyayama, *Jpn J Appl Phy* **50**, 09NE07 (2011)
63. O. Svitelskiy, J. Toulouse, G. Yong, Z.G. Ye, *Phys. Rev. B* **68**, 104107 (2003)
64. M. Wojdyr, *J. Appl. Crystall.* **43**, 1126 (2010)
65. T.A. Bennett, P.N. Kalu, A.D. Rollett, *Scr. Mater.* **57**, 41 (2007)
66. Y.M. Chiang, D. Birnie, W.D. Kingery *Physical Ceramics: Principles for Ceramic Science and Engineering.* (John Wiley & Sons, New York, 1997), pp. 351–513
67. R.M. German, *Sintering Theory and Practice* (Wiley, New York, 1996), p. 67
68. S.J.L. Kang, K.J. Yoon, *J. Eur. Ceram. Soc.* **5**, 135 (1989)
69. S.J.L. Kang *Sintering: Densification, Grain Growth & Microstructure.* (Elsevier Butterworth-Heinemann, Oxford, 2005), pp. 57–87
70. J.G. Fisher, A. Benčan, J. Godnjavec, M. Kosec, *J. Eur. Ceram. Soc.* **28**, 1657 (2008)
71. A. Zhang, R. Jing, M. Zhuang, H. Hou, L. Zhang, J. Zhang, X. Lu, Y. Yan, H. Du, L. Jin, *Ceram. Int.* **47**, 32747 (2021)
72. M. Lee *X-Ray Diffraction for Materials Research: From Fundamentals to Applications.* (Apple Academic Press Inc., Oakville, 2016), pp. 182–223
73. S. Kong, N. Kumar, S. Checchia, C. Cazorla, J. Daniels, *Adv. Funct. Mater.* **29**, 1900344 (2019)
74. S. Gorfman, P.A. Thomas, *J. Appl. Crystallogr.* **43**, 1409 (2010)
75. K. Reichmann, A. Feteira, M. Li, *Materials* **8**, 8467 (2015)
76. B.N. Rao, R. Datta, S.S. Chandrashekar, D.K. Mishra, V. Sathe, A. Senyshyn, R. Ranjan, *Phys. Rev. B* **88**, 224103 (2013)
77. A. Abbas, W.G. Jung, W.J. Moon, E. Uwiragiye, T.L. Pham, J.S. Lee, J.G. Fisher, W. Ge, F.U.H. Naqvi, J.H. Ko, *J. Korean Ceram. Soc.* **61**, 342 (2024)
78. J.-R. Gomah-Petry, S. Saïd, P. Marchet, J.-P. Mercurio, *J. Eur. Ceram. Soc.* **24**, 1165 (2004)
79. W.P. Cao, W.L. Li, X.F. Dai, T.D. Zhang, J. Sheng, Y.F. Hou, W.D. Fei, *J. Eur. Ceram. Soc.* **36**, 593 (2016)
80. S. Sayyed, S.A. Acharya, P. Kautkar, V. Sathe, *RSC Adv.* **5**, 50644 (2015)
81. J.R. Gomah-Petry, A.N. Salak, P. Marchet, V.M. Ferreira, J.P. Mercurio, *Physica Status Solidi (b)* **241**, 1949 (2004)
82. J.K. Lee, K.S. Hong, C.K. Kim, S.E. Park, *J. Appl. Phys.* **91**, 4538 (2002)
83. S.H. Oh, B.W. Lee, M. Jang, J.H. Ko, X. Li, H. Luo, *Curr. Appl. Phys.* **19**, 1195 (2019)
84. L. Luo, W. Ge, J. Li, D. Viehland, C. Farley, R. Bodnar, Q. Zhang, H. Luo, *J. Appl. Phys.* **109**, 113507 (2011)
85. J. Kreisel, A.M. Glazer, G. Jones, P.A. Thomas, L. Abello, G. Lucazeau, *J. Phys. Condens. Matter* **12**, 3267 (2000)
86. J. Petzelt, S. Kamba, J. Fábry, D. Noujni, V. Porokhonsky, A. Pashkin, I. Franke, K. Roleder, J. Suchanicz, R. Klein, G.E. Kugel, *J. Phys. Condens. Matter* **16**, 2719 (2004)
87. X. Liu, S. Xue, J. Ma, J. Zhai, B. Shen, F. Wang, X. Zhao, H. Yan, *J. Eur. Ceram. Soc.* **38**, 4631 (2018)
88. D. Rout, K.S. Moon, J. Park, S.J.L. Kang, *Curr. Appl. Phys.* **13**, 1988 (2013)
89. R. Roukos, S.A. Dargham, J. Romanos, D. Chaumont, *J. Alloys Compd.* **840**, 155509 (2020)
90. J. Wang, Z. Zhou, J. Xue, *Acta Mater.* **54**, 1691 (2006)
91. D. Rout, K.S. Moon, V.S. Rao, S.J.L. Kang, *J. Ceram. Soc. Jpn.* **117**, 797 (2009)
92. B. Wylie-van Eerd, D. Damjanovic, N. Klein, N. Setter, J. Trodahl, *Phys. Rev. B* **82**, 104112 (2010)

93. M. Eremenko, V. Krayzman, A. Bosak, H.Y. Playford, K.W. Chapman, J.C. Woicik, B. Ravel, I. Levin, *Nat. Commun.* **10**, 2728 (2019)
94. A. Bencan, E. Oveisi, S. Hashemizadeh, V.K. Veerapandiyam, T. Hoshina, T. Rojac, M. Deluca, G. Drazic, D. Damjanovic, *Nat. Commun.* **12**, 3509 (2021)
95. M.-H. Zhang, H.C. Thong, Y.X. Lu, W. Sun, J.-F. Li, K. Wang, *J. Korean Ceram. Soc.* **54**, 261 (2017)
96. S.M. Yang, Y. Kim, *J. Korean Ceram. Soc.* **56**, 340 (2019)
97. R. Dittmer, D. Gobeljic, W. Jo, V.V. Shvartsman, D.C. Lupascu, J.L. Jones, J. Rödel, *J. Appl. Phys.* **115**, 084111 (2014)
98. K.M. Kuruvila, V.V. Shvartsman, M. Hotari, D.A. Kiselev, N.V. Giridharan, *J. Appl. Phys.* **133**, (2023)
99. J.W. Hong, S.-I. Park, Z.G. Khim, *Rev. Sci. Instrum.* **70**, 1735 (1999)
100. E.Z. Luo, Z. Xie, J.B. Xu, I.H. Wilson, L.H. Zhao, *Phys. Rev. B* **61**, 203 (2000)
101. S. Ramazanov, F. Orudzhev, G. Gajiev, V. Holcman, R.S. Matos, H.D. da Fonseca Filho, Ş. Ṫalu, D. Selimov, *Appl. Surf. Sci.* **647**, 158863 (2024)
102. J.W. Hong, K.H. Noh, S.-I. Park, S.I. Kwun, Z.G. Khim, *Phys. Rev. B* **58**, 5078 (1998)
103. Pi UH, Kye Ji, Shin S, Khim ZG, Hong JW, Y. S, *J. Korean Phys. Soc.* **39**, 209 (2001)
104. S.-M. Cho, H.-J. Nam, B.H. Park, D.-Y. Jeon, *Ultramicroscopy* **108**, 1081 (2008)
105. R. Roth, M. Koch, J. Schaab, M. Liliensblum, F. Syrowatka, T. Band, T. Thurn-Albrecht, K. Dörr, *New J. Phys.* **20**, 103044 (2018)
106. J. Kling, X. Tan, W. Jo, H.J. Kleebe, H. Fuess, J. Rödel, *J. Am. Ceram. Soc.* **93**, 2452 (2010)
107. G.O. Jones, P.A. Thomas, *Acta Crystallogr. B* **58**, 168 (2002)
108. C.S. Tu, S.H. Huang, C.S. Ku, H.Y. Lee, R.R. Chien, V.H. Schmidt, H. Luo, *Appl. Phys. Lett.* **96**, 062903 (2010)
109. F. Cordero, F. Craciun, F. Trequatrini, E. Mercadelli, C. Galassi, *Phys. Rev. B* **81**, 144124 (2010)
110. W. Ge, C. Luo, Q. Zhang, C.P. Devreugd, Y. Ren, J. Li, H. Luo, D. Viehland, *J. Appl. Phys.* **111**, 093508 (2012)
111. V. Dorcet, G. Trolliard, P. Boullay, *Chem. Mater.* **20**, 5061 (2008)
112. W. Jo, S. Schaab, E. Sapper, L.A. Schmitt, H.J. Kleebe, A.J. Bell, J. Rödel, *J. Appl. Phys.* **110**, 074106 (2011)
113. S. Praharaj, D. Rout, V. Subramanian, S.J.L. Kang, *Ceram. Int.* **42**, 12663 (2016)
114. H.Y. Lee, K. Wang, F.Z. Yao, W. Sun, Z. Zhou, M.H. Zhang, X. Li, H. Luo, J.S. Lee, J.F. Li, *J. Appl. Phys.* **121**, 174103 (2017)
115. J.H. Park, S.J.L. Kang, *AIP Adv.* **6**, 015310 (2016)
116. Y. Noguchi, S. Teranishi, M. Suzuki, M. Miyayama, *J. Ceram. Soc. Jpn.* **117**, 32 (2009)
117. Y. Kitanaka, Y. Noguchi, M. Miyayama, *Phys. Rev. B* **81**, 094114 (2010)
118. N. Yasuda, N. Takahashi, N. Hidayah, H. Ohwa, O. Sakurada, Y. Tachi, K. Fujita, Y. Yamashita, M. Iwata, H. Terauchi, Y. Ishibashi, *J. Phys. Conf. Ser.* **320**, 012091 (2011)
119. Y. Kitanaka, T. Egawa, Y. Noguchi, M. Miyayama, *Jpn. J. Appl. Phys.* **55**, 10TB03 (2016)
120. W.R. Geng, X.H. Tian, Y.X. Jiang, Y.L. Zhu, Y.L. Tang, Y.J. Wang, M.J. Zou, Y.P. Feng, B. Wu, W.T. Hu, X.L. Ma, *Acta Mater.* **186**, 68 (2020)
121. U. Haselmann, Y.E. Suyolcu, P.-C. Wu, Y.P. Ivanov, D. Knez, P.A. Van Aken, Y.-H. Chu, Z. Zhang, *ACS Appl. Electron. Mater.* **3**, 4498 (2021)
122. L. He, D. Vanderbilt, *Phys. Rev. B* **68**, 134103 (2003)
123. L. Hong, A.K. Soh, Q.G. Du, J.Y. Li, *Phys. Rev. B* **77**, 094104 (2008)
124. K. Yamamoto, Y. Kitanaka, M. Suzuki, M. Miyayama, Y. Noguchi, C. Moriyoshi, Y. Kuroiwa, *Appl. Phys. Lett.* **91**, 162909 (2007)
125. H. Matsuo, Y. Noguchi, *Appl. Phys. Express* **15**, 081002 (2022)
126. L. Jin, F. Li, S. Zhang, *J. Am. Ceram. Soc.* **97**, 1 (2014)
127. M. Li, L. Li, J. Zang, D.C. Sinclair, *Appl. Phys. Lett.* **106**, 102904 (2015)

Publisher's Note Springer Nature remains neutral with regard to jurisdictional claims in published maps and institutional affiliations.

Springer Nature or its licensor (e.g. a society or other partner) holds exclusive rights to this article under a publishing agreement with the author(s) or other rightsholder(s); author self-archiving of the accepted manuscript version of this article is solely governed by the terms of such publishing agreement and applicable law.